3Y-TZP dip-coated with Zn-containing calcium silicate layers: development and characterization

Y. L. Bruni[1,2]*, M. P. Albano[1,2]

[1]Centro de Tecnología de Recursos Minerales y Cerámica, CCT-La Plata CONICET, CICPBA, CC 49 (B1897ZCA), M.B. Gonnet, Buenos Aires, Argentina

[2]Universidad Nacional de La Plata, Facultad de Ciencias Exactas, La Plata, Buenos Aires, Argentina

Abstract

Coating layers based on $Ca_3Si_3O_9$, $Ca_2ZnSi_2O_7$, and $ZnSiO_4$ on 3Y-TZP ceramics were obtained by the dip coating process, using SiO_2-CaO-P_2O_5-ZnO glass suspensions with Zn contents in the range of 0-20 mol%. The influence of the Zn content in the dip coating slips, the slip solid loading, and the 3Y-TZP surface porosity on the layer formation rate was studied. The Zn content of the dip coating slips as well as the slip solid loading greatly affected the slip viscosity, and consequently the liquid entrainment mechanism at the initial stage. The low dissolution rate of 20 mol% Zn-containing slips decreased the dip coating slip viscosity, whereas the lower stability of 10 mol% Zn-containing slips increased the slip viscosity. A significant increase in the initial layer thickness was produced either by using 10 mol% Zn-containing slips or by increasing the slip solid loading. The casting rate for longer immersion times was markedly accelerated by increasing the 3Y-TZP surface porosity. Sintered layers based on $ZnSiO_4$ having the lowest thickness values were produced using the glass containing 20 mol% Zn. On the other hand, the 0 and 10 mol% Zn-containing glass produced thicker sintered layers mainly composed of $Ca_3Si_3O_9$ and $Ca_2ZnSi_2O_7$, respectively.

Keywords: biomaterials, 3Y-TZP coated with Zn-containing calcium silicate, dip coating process, layer growth rate.

INTRODUCTION

Yttria-partially stabilized zirconia (3Y-TZP) is a ceramic widely used for dental and orthopedic applications owing to its excellent mechanical performance and biocompatibility [1, 2]. These properties combined with excellent aesthetics extended its application in dental crowns [3]. The use of Zn-containing glasses and glass-ceramics as coatings on 3Y-TZP is an approach to impart bioactive and antibacterial properties to the ceramic surface. Previous studies [4-6] have reported that Zn addition in silicate glasses retarded the glass degradation preventing bacterial infections. Zn is an essential component in the human bone and also stimulates bone formation *in vitro* and *in vivo*; in this sense, a Zn deficiency has been related to abnormal bone growth. In fact, Zn reduces bone resorption and accelerates the bone healing process, promoting osteoinductive properties [7-9]. One additional advantage of Zn-containing silicate glasses over Zn-free glasses is their superior mechanical strength [10]. Therefore, studies regarding the development and characterization of Zn-substituted calcium silicate ceramics, such as $Ca_2ZnSi_2O_7$, have been conducted in recent years [11, 12]. Several formulations of bioactive glasses doped with Zn have been obtained by the sol-gel method, and their *in vitro* bioactivity has been extensively studied [13, 14].

Ceramic layers on 3Y-TZP substrates can be developed by the dip coating process. The formation of a layer on the porous substrate surface by dip coating is a combination of the liquid entrainment mechanism at the initial stage, and the slip casting mechanism for dipping times >0. In this work, ceramic layers based on calcium silicate non-substituted and substituted by Zn with different thicknesses were obtained by immersing porous 3Y-TZP disks into SiO_2-CaO-P_2O_5-ZnO glass slips with Zn contents in the range of 0-20 mol%. The influence of the Zn content in the dip coating slips, the slip solid loading, and the 3Y-TZP surface porosity on the layer formation rate was investigated. Special emphasis was given to the Zn content of the dip coating suspensions and its influence on the thickness and composition of the sintered layer.

MATERIALS AND METHODS

Substrate preparation and characterization: 3Y-TZP disks were obtained by slip casting, using a commercial 3 mol% Y_2O_3 partially stabilized zirconia powder (d_{50}=0.40 μm, ZirPro, Saint-Gobain). 44 vol% aqueous 3Y-TZP slips were prepared in an ultrasonic bath, by dispersing the powder in distilled water with 0.4 wt% of ammonium polyacrylate dispersant (PN, Duramax D 3500, Rohm & Haas) at pH 9. Thereafter the slips were poured into molds to obtain green disks of 2 cm in diameter. The disks were dried at 100 °C for a day, followed by heating at 1000 and 1300 °C for 2 h with a heating rate of 10 °C.min^{-1}. The bulk density of the 3Y-TZP disks was measured by the ASTM C20 standard method. The relative density of 3Y-TZP was determined using a theoretical density value of 6.05 g/cm^3. The surface microstructure of the 3Y-TZP substrates was observed by scanning electron microscopy (SEM) using a Quanta 200 (FEI) microscope.

**yesibruni@hotmail.com*

https://orcid.org/0000-0002-0312-9251

Glass synthesis and characterization: three glasses with compositions $59SiO_2$-(36-x)CaO-$5P_2O_5$-xZnO (mol%), with x= 0, 10, and 20, were prepared by the sol-gel method. The different glasses were nominated as SCP-0Zn, SCP-10Zn, and SCP-20Zn in relation to their respective zinc content. Tetraethyl orthosilicate (TEOS) was added to 0.1 M HNO_3 solution to undergo acid hydrolysis; the mixture was magnetically stirred for 60 min. This was followed by the addition of triethyl phosphate (TEP), $Ca(NO_3)_2.4H_2O$, and $Zn(NO_3)_2.6H_2O$, with 45 min interval between each addition to allow each reagent to react. Finally, the whole mixture was further stirred for 60 min to complete the hydrolysis. The synthesized solution was saved in a sealed container for 10 days at room temperature until the gel was formed. Then, the gel was dried at 70 °C for 3 days and 110 °C for 2 days, followed by calcination at 700 °C for 24 h to eliminate residual nitrates and stabilize the glass phase. The stabilized glass powders were milled by attrition milling using isopropyl alcohol for 3 h to obtain an average particle diameter of 3.0 μm. Afterward, the powder was dried at 60 °C for 24 h. The crystalline phases were analyzed by powder X-ray diffraction (XRD), using a diffractometer (D2, Brucker) with CuKα radiation and Ni filter in the 15-60º 2θ range. Differential thermal analysis (DTA) of the glass powders was carried out in the air, using a thermal analyzer (STA 409, Netzsch) at a heating rate of 10 °C.min^{-1}. The BET surface area (S_{BET}) and the pore size distribution curves of the stabilized glass powders were evaluated using a pore analyzer (ASAP 2020, Micromeritics).

Processing of glass slips and dip coating: dip coating of SCP-0Zn, SCP-10Zn, and SCP-20Zn slips with different solid loading (10 and 15 vol%) were prepared in an ultrasonic bath, using 0.4 wt% PN as dispersant and 5 wt% polyvinyl alcohol as a binder. Steady flow curves of shear stress versus shear rate were obtained using a concentric cylinder viscometer (VT550, Haake) at room temperature. A coaxial cylinder system with two gaps (sensor system NV, Haake) was used. Zeta potential as a function of pH curves were determined for 0.06 vol% suspensions with 0.4 wt% PN at pH 3-12. HCl or NH_4OH solutions were used to adjust the pH. 10 and 15 vol% glass slips with different compositions were allowed to settle under gravity for 3 days to determine the maximum packing fraction (ϕ_m) as follows:

$$\emptyset_m = \frac{C}{1 - (H_l/H_t)} \quad (A)$$

where H_l is the liquid height above the solid sediment, H_t is the total height of the suspension, and C is the volume fraction of solids. 3Y-TZP disks were dipped into glass slips for different times at a constant immersion and withdrawal rate of 6 mm/s. The coated discs were dried at room temperature and then at 100 °C. Finally, the sintered layers were obtained by heating at 1000 °C for 1 h. Sections polished with diamonds of coated 3Y-TZP disks were characterized by SEM. The sintered layer thickness was measured on different sites along the 3Y-TZP surface, and the reported thickness values were the average of at least thirty measurements.

RESULTS AND DISCUSSION

Substrate and glass characterization

The porosity of 3Y-TZP disks sintered at 1000 °C was 46.76%; a lower porosity of 21.80% was measured at 1300 °C, as expected. SEM micrographs of the top and bottom surfaces of 3Y-TZP sintered at 1000 °C are shown in Fig. 1. During casting, the top surface was exposed to the atmosphere whereas the bottom one was in contact with the mold. The bottom surface appeared rough as a consequence of the roughness of the mold in contrast to the smooth top surface. Another difference between both surfaces was the coarser microstructure of the bottom one. As we have previously pointed out [15], this can be attributed to the settling of the large particles at the bottom surface during casting. Accordingly, the migration of the fine particles to the top surface resulted in a finer microstructure.

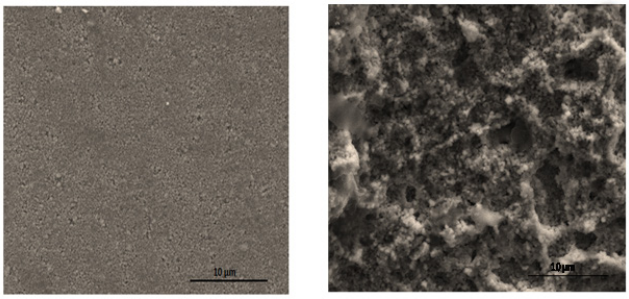

Figure 1: SEM micrographs of the top (a) and bottom (b) surfaces of 3Y-TZP sintered at 1000 °C.

The XRD patterns of the three glasses calcined at 700 °C (Fig. 2a) showed a broad and diffused band at 17-25° 2θ attributed to the amorphous SiO_2 network, confirming the amorphous nature of the obtained glasses. However, poorly crystalline main phases were also detected in all the glasses as a consequence of the partial crystallization, which took place during heating at 700 °C. They corresponded to the formation of $Ca_3Si_3O_9$ (JCPDS 74-0874) for SCP-0Zn, Ca_2ZnSiO_7 (JCPDS 12-0453) for SCP-10Zn, and $ZnSiO_4$ (JCPDS 37-1485) for SCP-20Zn. The presence of Ca_2ZnSiO_7 and $ZnSiO_4$ in SCP-10Zn and SCP-20Zn, respectively, indicated that the Zn content in silicates increased at the expense of Ca. The XRD patterns of the glass powders sintered at 1000 °C are shown in Fig. 2b. The main crystalline phase for SCP-0Zn was $Ca_3Si_3O_9$, this one was accompanied by a secondary crystal phase of β-$CaSiO_3$ and a small amount of amorphous SiO_2. The 10 mol% Zn-containing glass produced Ca_2ZnSiO_7 as a major crystalline phase, along with minor amounts of quartz (JCPDS 85-0794) and cristobalite (JCPDS 71-0785) traces. The composition of SCP-20Zn showed the presence of $ZnSiO_4$ and cristobalite; in addition to these phases, a small quantity of quartz and Ca_2ZnSiO_7 traces were detected. The diffraction peak of cristobalite at 2θ=21.95° [(101) atomic

plane] was overlapped with that of $ZnSiO_4$ [(330) atomic plane]. The increase in the Zn content from 10 to 20 mol% enhanced the formation of Zn-rich phases, and also promoted the appearance of cristobalite at the expense of quartz.

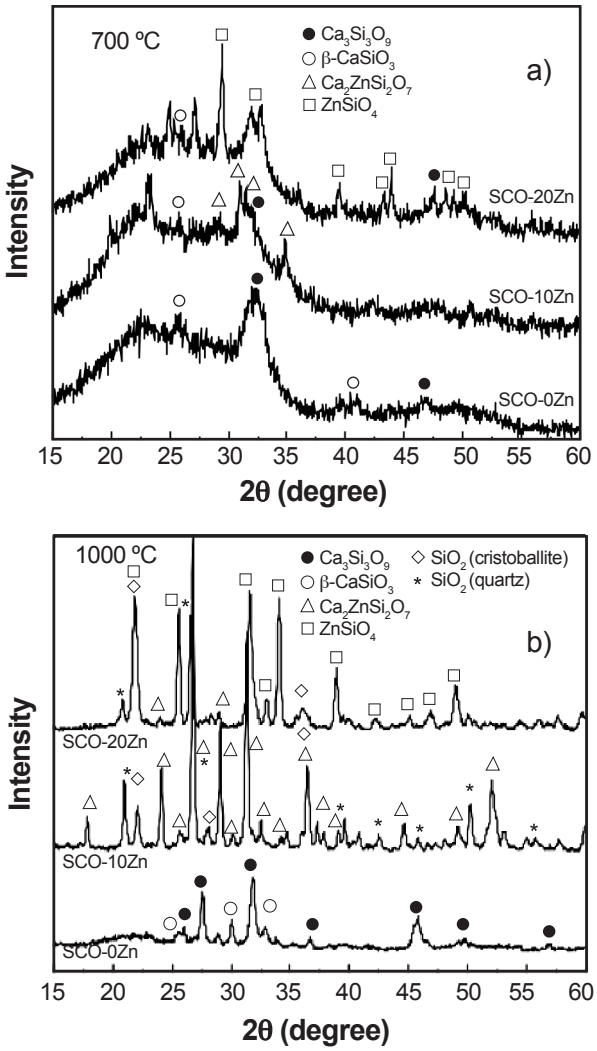

Figure 2: XRD patterns of the different glasses calcined at 700 °C (a) and sintered at 1000 °C (b).

The crystallization process of the glasses was analyzed by DTA. The DTA curves of the stabilized glass powders are shown in Fig. 3. Weak endothermic peaks corresponding to the glass transition and stronger ones associated with the fusion of crystalline phases appeared; the exothermic peaks corresponded to glass crystallization. The endothermic peaks that appeared at 100 °C in all the glasses were associated with water loss. As the Zn content increased from 0 to 10 mol% the glass transition temperature (T_g) values decreased from 790 to 760 °C. A greater Zn addition of 20 mol% increased T_g to 819 °C. For SCP-0Zn, the exothermic peaks at 863 and 903 °C can be respectively assigned to the crystallization of β-$CaSiO_3$ and $Ca_3Si_3O_9$. In the case of Zn-containing glasses, the exothermic peak at 858 °C corresponded to Ca_2ZnSiO_7 crystallization for SCP-10Zn, and the broad exothermic peak centered at 1035 °C for SCP-20Zn was produced by the overlapping of the $ZnSiO_4$ and cristobalite peaks. The effect of Zn addition on the T_g values was closely related to the structural role of Zn in the glass powders. Several researchers [11-13, 16] reported that the partial substitution of Ca by Zn in the reference glass (SCP-0Zn) produced modifications in the glass network connectivity. When the Zn acts as network former, it generates a more stable structure due to its incorporation into the glass network through covalent links between SiO_4 tetrahedrons, increasing the number of bridging oxygen (BO) bonds. Zn^{2+} bivalent cations can be incorporated into the silicate network, forming Si-O-Zn bonds with two orthosilicate radical neighbors, according to the reaction:

$$Si\text{-}O\text{-}Si + ZnO \rightarrow Si\text{-}O\text{-}Zn\text{-}O\text{-}Si \qquad (B)$$

The greater network connectivity results in an increase in T_g. On the contrary, when the Zn plays the role of network modifier, it reduces the network connectivity by the increase of non-bridging oxygen (NBO) bonds and decreases the T_g value. Based on this discussion, our findings suggested that Zn acted as a network former in SCP-20Zn and a network modifier in SCP-10Zn.

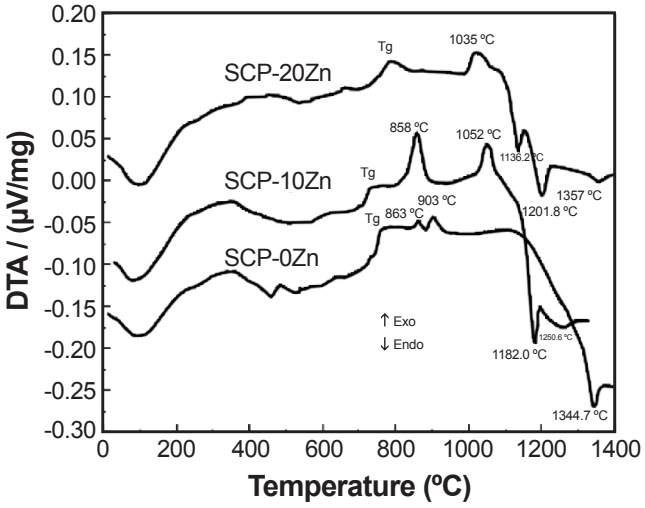

Figure 3: DTA curves of the stabilized glass powders.

Fig. 4 shows the nitrogen adsorption isotherm and the pore size distribution curves of the different glasses. The BET surface area (S_{BET}) and the total pore volume (V_p) of the glasses are, respectively, included in Figs. 4a and 4b. The curves in Fig. 4a corresponded to type IV isotherms which are characteristics of a mesoporous structure. The porous structure of the glasses was generated by the gel formation process, in which the hydrolyzed precursors were linked by condensation. The evaporation of water and ethanol, retained in the capillaries of the structure, and the nitrate decomposition during heating contributed to the glass porosity. The glasses showed unimodal pore size distribution curves between 2 and 50 nm (Fig. 4b). Similar more frequent pore sizes in the range of 17.5 to 22 nm were found for the different glass compositions. The textural parameters

depended on the zinc addition. The 10 mol% Zn-containing glass exhibited a more porous network and consequently the largest S_{BET}. A similar effect has been previously reported by the low incorporation of Zn in mesoporous SiO_2-CaO glasses [17, 18]. In contrast, the addition of 20 mol% Zn did not induce a substantial change in the textural parameters with respect to the reference glass without Zn. Thus, the textural parameter results confirmed the structural role of Zn in the glasses. In SCP-10Zn, Zn assumed the role of a network modifier breaking the atomic array of SiO_4^{4-} structural units and generating defects and pores. This behavior was not found for SCP-20Zn since the Zn acted as a network former.

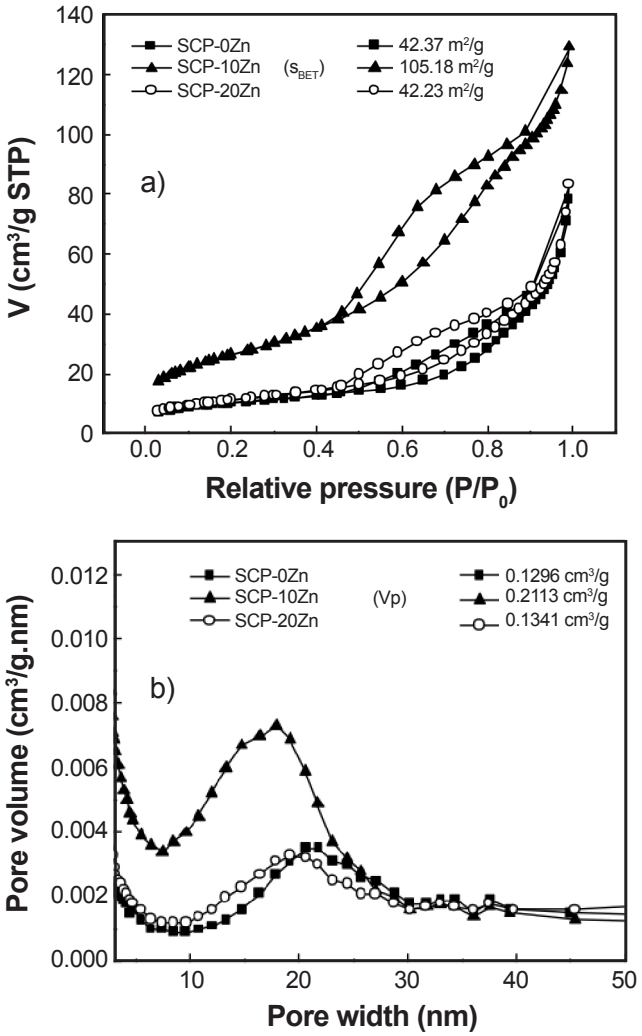

Figure 4: Nitrogen adsorption isotherm (a) and pore size distribution (b) curves of the different glasses.

Slip properties of glass coating

Fig. 5 shows the flow curves of viscosity as a function of shear rate for different glass compositions and solid loading. The viscosity of the coating slips significantly varied with the glass composition. This variation became greater with increasing the slurry solid loading. For each solid loading, the 10 mol% Zn-containing glass slips showed the highest viscosity; on the contrary, the incorporation of 20 mol% Zn produced well-dispersed slips having the lowest viscosity values. The carboxylate groups negatively charged ($RCOO^-$) of the PN polyelectrolyte at pH 8.5 was adsorbed at the particle surface. The magnitude of the polyelectrolyte adsorption depends on the pH and the ionic strength of the suspensions. In order to get insight into the ionic strength of the slurries, the pH change with increasing glass concentration during the aqueous colloidal processing of 10 vol% SCP-0Zn, SCP-10Zn, and SCP-20Zn slips is presented in Table I. A pH increment from 7.00 to 9.32, 10.00, and 8.60 was measured with the introduction of about 0.04 g/mL of SCP-0Zn, SCP-10Zn, and SCP-20Zn, respectively, to the aqueous solution. The pH remained nearly constant with further glass additions. It is well known [19-21] that the increase in pH upon immersion of glass to the aqueous solution can be related to an exchange reaction between H^+ from the solution and modifier cations (located at NBO bonds) from the glass. This exchange reaction produces cations leached out from the glass surface and OH^-, leading to an increase in pH [19-21]. The smaller variation of pH in SCP-20Zn glass solutions indicated a lower cation release rate from the glass surface. A marked reduction in cation release from 45S5 glass with the substitution of Ca by Zn at pH ~7 has been reported elsewhere [5, 6]. In our study, the glass dissolution and the ion exchange reaction decreased with increasing the network connectivity. It has also been reported [14, 22] that in glasses with a Zn content higher than 10 mol%, the Ca^{2+} could be removed from NBO bonds by electrostatic forces derived from the presence of ZnO_4^{2-} ions in the structure. In our study, the greater network connectivity and the capture of Ca^{2+} from NBO bonds could be responsible for the decrease in SCP-20Zn dissolution rate. On the other hand, a higher dissolution rate of SCP-10Zn with the corresponding increase in pH was found. Comparing SCP-10Zn with SCP-0Zn, a similar ion-exchange reaction could be expected since Ca^{2+} in NBO bonds was replaced by Zn^{2+}. However, the significantly higher S_{BET} and V_p of SCP-10Zn, with

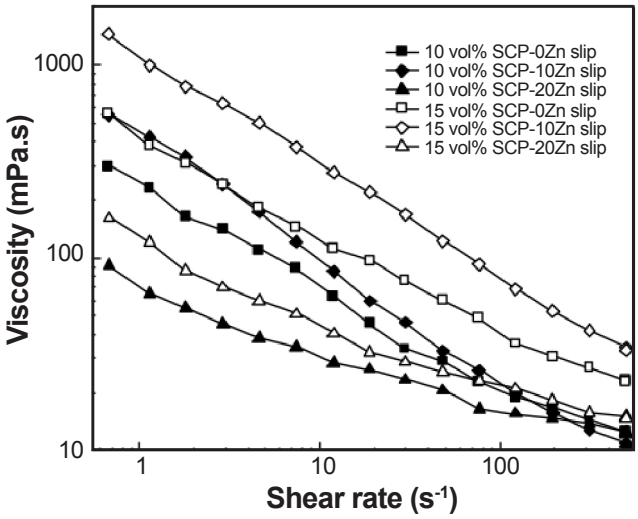

Figure 5: Flow curves of viscosity as a function of shear rate for different glass compositions and solid loadings.

Table I - pH as a function of glass concentration during the aqueous colloidal processing of different 10 vol% slips.

Glass concentration (g/mL)	SCP-0Zn	SCP-10Zn	SCP-20Zn
0	7.00	7.00	7.00
0.040	9.32	10.00	8.60
0.078	9.30	9.99	8.58
0.122	9.29	10.03	8.61
0.180	9.31	10.01	8.59
0.253	9.30	10.02	8.62

respect to those of SCP-0Zn, indicated a more open silicate network, which promoted the ion exchange reaction. SCP-0Zn exhibited an intermediate glass dissolution rate between that of SCP-10Zn and SCP-20Zn.

In the colloidal processing of diluted 10 and 15 vol% slips, the separation distance between particles was large. In this condition, the electrostatic forces between particles provided by the PN adsorption could be considered as the main contribution to the slip stabilization. Some researchers [23, 24] have studied the Ca^{2+} effect on the adsorption of poly(acrylic acid) (PAA) dispersant on oxide surface, reporting that Ca^{2+} formed chemical complexes with PAA in the adsorbed polyacrylate layer. These complexes reduce the electrostatic charge of the adsorbed polymer and promote the $RCOO^-$ adsorption [24-26]. Therefore, the formation of complexes in the adsorbed layer increases the polymer adsorption leading to thick layers. In our study, the Ca^{2+} and Zn^{2+} leached out from the glass surface could form complexes with PN in the adsorbed layer, altering the net surface charge of the PN adsorbed-glass powders. Fig. 6 shows the curves of zeta potential as a function of pH of the different glass slips with 0.4 wt% PN. SCP-20Zn slip exhibited the highest negative zeta potential value in the alkaline pH range. This behavior was in accordance with the lower dissolution of SCP-20Zn glass (Table I). The lower cation release of SCP-20Zn could result in thinner adsorbed layers with a higher net surface charge. The increase in the electrostatic repulsive interactions between particles led to low viscosity values of 10 and 15 vol% SCP-20Zn slips. On the contrary, the higher Ca^{2+} and Zn^{2+} released from the SCP-10Zn surface produced thicker layers having lower net surface charge (Fig. 6).

The high S_{BET} of SCP-10Zn glass powders could also contribute to increasing the slip viscosity. In general, the effective solid volume fraction of powders with high S_{BET} is greater than the calculated volume fraction of solid, as a consequence of thicker hydrated and polyelectrolyte adsorbed layers [27]. In order to confirm this hypothesis, the values of maximum packing fraction (ϕ_m) for 10 and 15 vol% SCP-0Zn, SCP-10Zn, and SCP-20Zn slips were determined and presented in Table II. The lowest ϕ_m value for SCP-10Zn slips at both solids loading indicated a higher solid sediment volume (Eq. A). Therefore, a larger

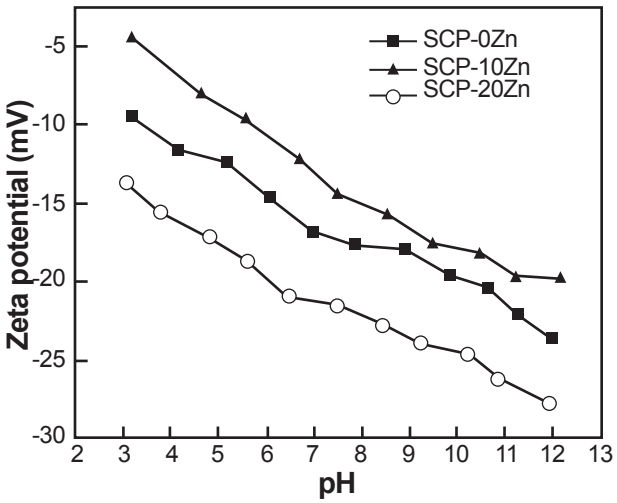

Figure 6: Zeta potential as a function of pH of the different glass slips with 0.4 wt% PN.

effective solid volume fraction of SCP-10Zn relative to that of SCP-0Zn and SCP-20Zn could be assumed. The lower electrostatic repulsion between particles together with the higher effective solid volume fraction of SCP-10Zn slips produced an increase in the slip viscosity. For each glass composition, the slip viscosity increased as the solid loading increased from 10 to 15 vol% due to greater particle and hydrodynamic interactions.

Table II - Maximum packing fraction, ϕ_m (%), as a function of the slip composition and solid loading.

Slip solid loading (vol%)	SCP-0Zn	SCP-10Zn	SCP-20Zn
10	12.5	10.6	13.7
15	18.7	15.4	20.3

Dip coating layers

During the dip coating process, the flat substrate was immersed into the coating slip for different times; afterward, it was withdrawn from the suspension, leaving a layer on its surface. The initial stage of the dip coating process is known as the liquid entrainment mechanism. The initial thickness of the adhered layer (H_0) at a constant withdrawn speed (v) can be expressed as the ratio between the viscous forces and the liquid surface tension (γ) by [28-30]:

$$H_0 = C\left(\frac{\eta.v}{\gamma}\right)^{2/3} \quad (C)$$

where C is a constant and η is the slip viscosity. A thin ceramic coating on the substrate surface was formed after the liquid evaporation from the adhered layer. At longer immersion times, the capillary filtration of the liquid through the pores on the sample surface generated a wet cake at the suspension-substrate interface. The final sintered film was

obtained after heat treatment of the coated substrate. The layer growth under the capillary filtration driving force can be satisfactorily described by the slip casting model. Based on this model, the evolution of the sintered layer thickness (H_s) with time is given by [28]:

$$H_s = a\left(\frac{\varepsilon.\gamma.K.t}{\mu.\beta.r}\right)^{1/2} \quad (D)$$

where a and β are expressed as:

$$a = \frac{\varphi}{(1-\varepsilon_s)} \quad (E)$$

$$\beta = \left(\frac{\varphi}{\varphi_1}\right) - 1 \quad (F)$$

where ϕ is the volume fraction of particles in the coating slip, ϕ is the volume fraction of particles in the wet layer, ε is the porosity of the substrate, ε_s is the porosity of the sintered layer, μ is the viscosity of the dispersion liquid, r is the pore radius, K is the wet layer permeability, and t is the dipping time. According to Eq. D, the solid content of the slips, the substrate porosity, and the layer permeability have an important influence on the layer growth rate. Fig. 7a shows the experimental thickness of the sintered layer on the smooth surfaces as a function of dipping time for 3Y-TZP sintered at 1000 and 1300 °C dip-coated in different suspensions. The layer thickness increased with dipping time up to reaching surface saturation at 120 s. The thickest layer at 120 s (54 μm) was obtained for 3Y-TZP sintered at 1000 °C dip-coated in 15 vol% SCP-10Zn slip. On the other hand, the thinnest layer (17 μm) was found for 3Y-TZP sintered at 1300 °C immersed in 10 vol% SCP-20Zn slip. It can be noticed that for the same substrate and slip solid loading, the casting rate markedly varied with the Zn glass content. For 3Y-TZP sintered at 1000 °C dip-coated in 15 vol% slips, layer thickness about 50% smaller was formed using SCP-20Zn dip coating slip in comparison to SCP-10Zn slip. The same tendency was found in the case of 3Y-TZP sintered at 1300 °C dip-coated in 10 vol% slips with different glass compositions; thus the layer growth rate was strongly dependent on the Zn content.

SEM images of 3Y-TZP sintered at 1000 °C dip-coated in 10 vol% SCP-10Zn and SCP-20Zn slips during 120 s (Fig. 8) confirmed the layer thickness results. Clearly, a lower layer thickness was obtained by using SCP-20Zn dip coating slips. Fig. 7b presents the squared layer thickness versus dipping time for 3Y-TZP sintered at 1000 and 1300 °C dip-coated in different suspensions. The linear relation between the squared layer thickness and time indicated that the layer formation for t>0 followed the slip casting model (Eq. D). As mentioned, the first mechanism in the layer formation process (dipping time ~0) was the liquid entrainment, which left a thin slurry film on the substrate surface. The initial layer thickness (H_0) was the intersection of the lines with the squared layer thickness axis in Fig. 7b. For identical substrate and slip solid loading, H_0 varied with the Zn concentration of the dip coating slurries. The disks immersed in SCP-10Zn slips exhibited the highest initial layer thickness and the lowest one was found for SCP-20Zn slips, having SCP-0Zn slips an intermediate H_0 value. According to Eq. C, at a constant withdrawn rate, H_0 was only influenced by the slip viscosity. Therefore, the variation of the initial thickness values with the Zn content of dip coating slips was in agreement with their respective slip viscosity values (Fig. 5). The lower viscosity of 20 mol% Zn-containing slips produced thinner initial layers, whereas 10 mol% Zn-containing slips having the highest viscosity resulted in thicker layers at the initial stage. Considering dipping times >0 in Fig. 7b, the 10 mol% Zn-containing glass slip presented a slightly greater casting rate (greater line slope) in comparison to 0 and 20 mol% Zn-containing slips, for the same substrate and slip solid loading. This result could be attributed to the lower ϕ_m value of 10 mol% Zn-containing slips, which increased the permeability and porosity of the wet layer, resulting in a higher casting rate (Eq. D).

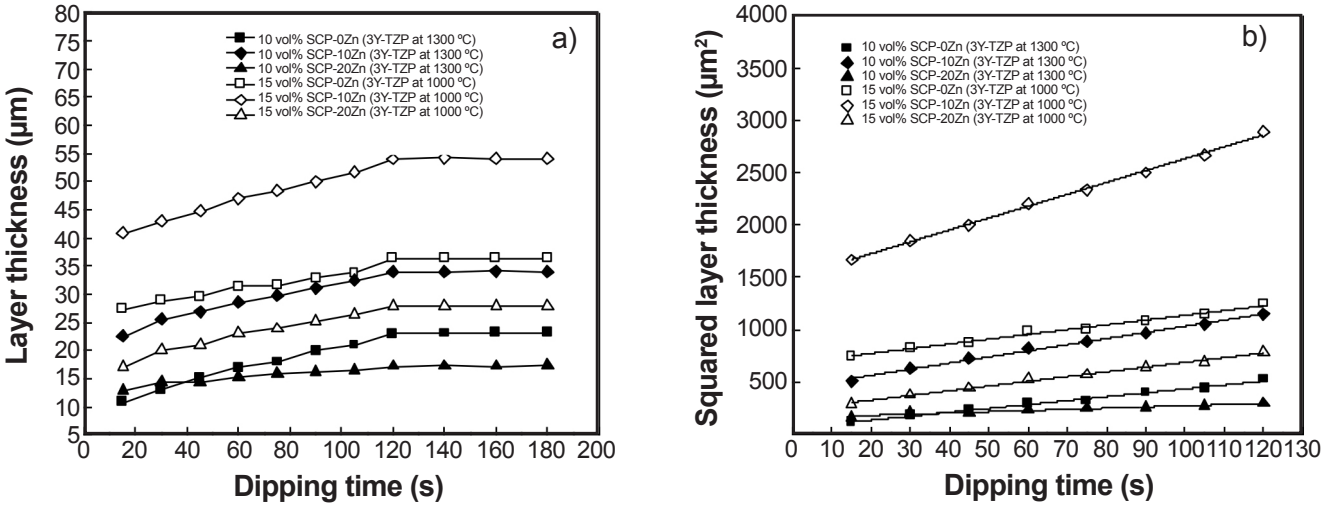

Figure 7: Linear (a) and squared (b) layer thickness on the smooth surfaces as a function of dipping time for 3Y-TZP sintered at 1000 and 1300 °C dip-coated in different suspensions.

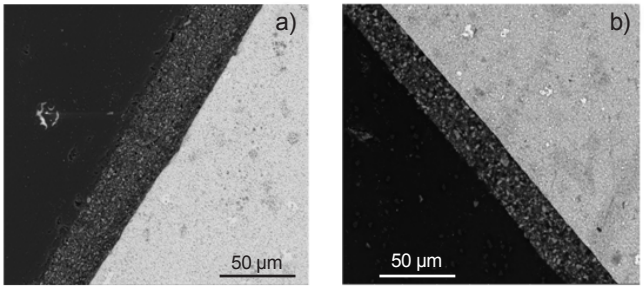

Figure 8: SEM images of 3Y-TZP samples sintered at 1000 °C dip-coated in different 10 vol% slips during 120 s showing the surface layers formed with SCP-10Zn (a) and SCP-20Zn (b) glass powders.

The effect of the 3Y-TZP surface porosity and the slip solid loading on the layer formation rate is shown in Fig. 9. As expected, identical slips and consequently slip viscosity produced layers with similar initial thickness irrespective of the 3Y-TZP surface porosity. However, the surface porosity of the substrate greatly affected the casting rate for longer immersion times. The greater surface porosity of 3Y-TZP sintered at 1000 °C markedly increased the casting rate (Eq. D). On the other hand, when the same substrate was used, a greater thickness at the initial stage was formed by increasing the slip solid loading. This behavior was attributed to the higher viscosity of 15 vol% slips relative to that of 10 vol% slips (Fig. 5). However, the casting rate for longer dipping times was not significantly altered with the increase in the slip solid content from 10 to 15 vol%. It was expected that these stable suspensions produced a wet layer with similar permeability and therefore casting rate. In summary, a significant increase in the initial layer thickness was produced either by increasing the slip solid content or by using 10 mol% Zn-containing glass slips. The casting rate was markedly accelerated by increasing the 3Y-TZP surface porosity. A notable increase in the initial layer thickness followed by a less pronounced increase in the casting rate

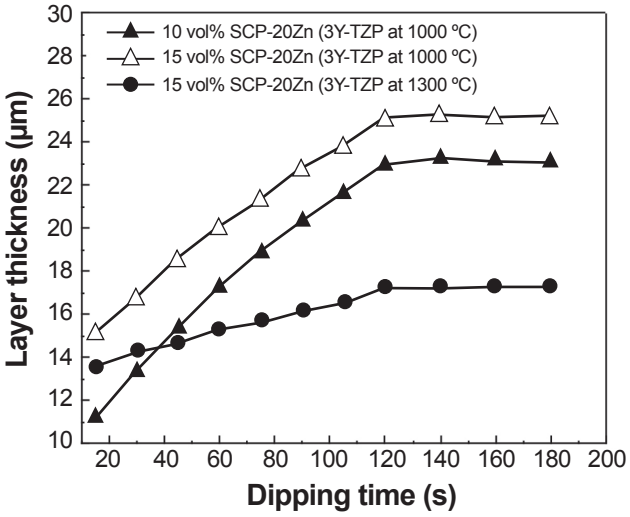

Figure 9: Layer thickness on the smooth surfaces as a function of dipping time for 3Y-TZP sintered at 1000 °C dip-coated in SCP-20Zn slips with different solid loading, and 3Y-TZP sintered at different temperatures dip-coated in 15 vol% SCP-20Zn slip.

was found when 3Y-TZP was dip-coated in 10 mol% Zn-containing glass slips.

CONCLUSIONS

Coating layers based on $Ca_3Si_3O_9$, $Ca_2ZnSi_2O_7$, and $ZnSiO_4$ on 3Y-TZP ceramics were developed by the dip coating process. The influence of the Zn content in the dip coating slips, the slip solid concentration, and the 3Y-TZP surface porosity on the layer formation rate was evaluated. The Zn content of the dip coating slips as well as the slip solid loading greatly affected the slip viscosity, and consequently the liquid entrainment mechanism at the initial stage. The low dissolution rate of 20 mol% Zn-containing slips markedly decreased the dip coating slip viscosity. Thinner initial layers were found either by using 20 mol% Zn-containing slips or by decreasing the slip solid loading. For longer dipping times, the casting rate decreased by reducing the 3Y-TZP surface porosity. The glass containing 20 mol% Zn produced sintered layers mainly composed of $ZnSiO_4$, having the lowest thickness values. On the other hand, the 10 mol% Zn-containing slips produced thicker layers based on $Ca_2ZnSi_2O_7$. $Ca_2ZnSi_2O_7$ and $ZnSiO_4$ coatings on 3Y-TZP would play an important role in wound healing, becoming promising ceramics for orthopedic and dental applications.

REFERENCES

[1] F. Chen, J.M. Wu, H.Q. Wu, Y. Chen, C.H. Li, Y.S. Shi, Int. J. Lightweight Mater. Manuf. **1** (2018) 239.
[2] Y. Zhang, B.R. Lawn, J. Dent. Res. **97** (2017) 1.
[3] C.H. Chin, A. Muchtar, C. Azhari, M. Razali, M. Aboras, Malaysian J. Anal. Sci. **20** (2016) 642.
[4] S.M. Rabiee, N. Nazparvar, M. Azizian, D. Vashaee, L. Tayebi, Ceram. Int. **41** (2015) 7241.
[5] M. Blochberger, L. Hupa, D. Brauer, Biomed. Glasses **1** (2015) 93.
[6] G.S. Lázaro, S.C. Santos, C.X. Resende, E.A. Santos, J. Non-Cryst. Solids **386** (2014) 19.
[7] M. Yamaguchi, K. Inamoto, Y. Suketa, Biochem. Pharmacol. **36** (1987) 4007.
[8] M. Yamaguchi, K. Inamoto, Y. Suketa, Res. Exp. Med. **186** (1986) 337.
[9] S.A. Seyedmajidi, M. Seyedmajidi, A. Moghadamnia, Dent. Res. J. **11** (2014) 475.
[10] A. Karthika, L. Kavitha, M. Surendiran, S. Kannan, D. Gopi, RSC Adv. **5** (2015) 47341.
[11] J. Ma, B.X. Huang, X.C. Zhao, C.Z. Wang, Ceram. Int. **43** (2017) 14851.
[12] J. Ma, B.X. Huang, X.C. Zhao, X.H. Hao, C.Z. Wang, Mater. Lett. **236** (2019) 566.
[13] I. Atkinson, E.M. Anghel, L. Predoana, O.C. Mocioiu, L. Jecu, I. Raut, C. Munteanu, D. Culita, M. Zaharescu, Ceram. Int. **42** (2016) 3033.
[14] A. Balamurugan, G. Balossier, S. Kannan, J. Michel, A.H.S. Rebelo, J.M.F. Ferreira, Acta Biomater. **3** (2007) 255.
[15] Y.L. Bruni, L.B. Garrido, M.P. Albano, L.N. Teixeira,

P.T. de Oliveira, A.L. Rosa, Ceram. Int. **41** (2015) 14212.
[16] M. Abeer, El-Kady, F.A. Ashraf, Ceram. Int. **38** (2012) 1195.
[17] A.J. Salinas, S. Shruti, G. Malavasi, L. Menabue, M. Vallet-Regí, Acta Biomater. **7** (2011) 3452.
[18] L. Courtheoux, J. Lao, J.M. Nedelec, E. Jallot, J. Phys. Chem. C **112** (2008) 13663.
[19] M. Bini, S. Grandi, D. Capsoni, E. Saino, L. Visai, J. Phys. Chem. C **113** (2009) 8821.
[20] S. Kapoor, A. Goel, A. Tilocca, V. Dhuna, G. Bhatia, K. Dhuna, J.M.F. Ferreira, Acta Biomater. **10** (2014) 3264.
[21] J.E. Shelby, *Introduction to glass science and technology*, 2nd ed., Royal Soc. Chem. (2005).
[22] S. Shahrabi, S. Hesaraki, S. Moemeni, M. Khorami, Ceram. Int. **37** (2011) 2737.
[23] J.A. Lewis, J. Am. Ceram. Soc. **83** (2000) 2341.
[24] L. Dupont, A. Foissy, R. Mercier, B. Mottet, J. Colloid Interf. Sci. **161** (1993) 455.
[25] J. Sun, L. Bergstrom, L. Gao, J. Am. Ceram. Soc. **84** (2001) 2710.
[26] N. Sebastian, B. George, B. Mathew, Polym. Degrad. Stab. **60** (1998) 371.
[27] G. Tari, M.F. Ferreira, O. Lyckfeldt, J. Eur. Ceram. Soc. **18** (1998) 479.
[28] Y. Gu, G. Meng, J. Eur. Ceram. Soc. **19** (1999) 1961.
[29] C.J. Brinker, G.C. Frye, A.J. Hurd, C.S. Ashley, Thin Solid Films **201** (1991) 97.
[30] T. Schneller, R. Wasser, M. Kosec, D. Payne (Eds.), "Chemical solution deposition of functional oxide thin films", Springer-Verlag (2013).
(Rec. 20/04/2021, Rev. 12/07/2021, Ac. 16/07/2021)

Cerâmica

Ano LXVII - Vol 67, 384 OUT/NOV/DEZ 2021 - ISSN-0366-6913